Available online at www.sciencedirect.com
ScienceDirect
Journal of Magnesium and Alloys xxx (xxxx) xxx
www.elsevier.com/locate/jma

Full Length Article

Corrosion and in *vitro* cytocompatibility investigation on the designed Mg-Zn-Ag metallic glasses for biomedical application

Jian Wang[a,b], Lingzhong Meng[a], Weixin Xie[c], Chen Ji[a], Ronghua Wang[d], Pinghu Zhang[d,*], Liling Jin[e], Liyuan Sheng[f,g,*], Yufeng Zheng[f]

[a] *School of Mechanical Engineering, Yangzhou University, Yangzhou, 225127, China*
[b] *Department of Materials Science and Engineering, Seoul National University, Seoul, South Korea*
[c] *Huizhou Port Customs, Huizhou, 516081, China*
[d] *Jiangsu Key Laboratory of Integrated Traditional Chinese and Western Medicine for Prevention and Treatment of Senile Diseases, Institute of Translational Medicine, Medical College, Yangzhou University, Yangzhou, 225009, China*
[e] *Center for Research in Computational Thermochemistry (CRCT), Department of Chemical Engineering, Ecole polytechnique de Montréal, Montréal, Québec, H3C 3A7, Canada*
[f] *Shenzhen Institute, Peking University, Shenzhen 518057, China*
[g] *PKU-HKUST ShenZhen-HongKong Institution, Shenzhen, 518057, China*

Received 7 June 2022; received in revised form 8 September 2022; accepted 21 September 2022
Available online xxx

Abstract

In the present work, seven Mg-Zn-Ag alloys with the nominal composition of $Mg_{96-x}Zn_xAg_4$ ($x = 17$, 20, 23, 26, 29, 32, 35 in at.%) were prepared by induction melting and single-roller melt-spinning. The X-ray diffraction (XRD) analyses indicate the metallic glasses with three composition of $Mg_{73}Zn_{23}Ag_4$, $Mg_{70}Zn_{26}Ag_4$, and $Mg_{67}Zn_{29}Ag_4$ were obtained successfully. The differential scanning calorimetry (DSC) measurement was used to obtain the characteristic temperature of Mg-Zn-Ag metallic glasses for the glass-forming ability analysis. The maximum glass transition temperature (T_{rg}) was found to be 0.525 with a composition close to $Mg_{67}Zn_{29}Ag_4$, which results in the best glass-forming ability. Moreover, the immersion test in simulated body fluid (SBF) demonstrate the relative homogeneous corrosion behavior of the Mg-Zn-Ag metallic glasses. The corrosion rate of Mg-Zn-Ag metallic glasses in SBF solution decreases with the increase of Zn content. The sample $Mg_{67}Zn_{29}Ag_4$ has the lowest corrosion rate of 0.19 mm/yr, which could meet the clinical application requirement well. The in vitro cell experiments show that the Madin-Darby canine kidney (MDCK) cells cultured in sample $Mg_{67}Zn_{29}Ag_4$ and its extraction medium have higher activity. However, the Mg-Zn-Ag metallic glasses exhibit obvious inhibitory effect on human rhabdomyosarcoma (RD) tumor cells. The present investigations on the glass-forming ability, corrosion behavior, cytocompatibility and tumor inhibition function of the Mg-Zn-Ag based metallic glass could reveal their biomedical application possibility.

Keywords: Metallic glasses; Mg-Zn-Ag; Corrosion behavior; In vitro cytocompatibility.

1. Introduction

Magnesium (Mg) alloys have excellent biocompatibility (no toxicity), good biodegradability, low density (1.74–2.0 g/cm^3), and moderate Young's modulus close to the human bone. Therefore, they have been considered as one of the most potential candidates for biomedical application [1,2]. Actually, Mg is an essential element in the human body, as it is involved in a series of metabolic processes [3]. Redundant Mg ions with appropriate concentration would not cause any adverse effect, as they are excreted in the urine. However, the corrosion rates of the normal Mg-based alloys in body fluids are extremely high, which could influence the tissue activity and result in insufficient mechanical strength before

* Corresponding authors.
E-mail addresses: zhangpinghu@yzu.edu.cn (P. Zhang), lysheng@yeah.net (L. Sheng).

https://doi.org/10.1016/j.jma.2022.09.025

Please cite this article as: J. Wang, L. Meng, W. Xie et al., Corrosion and in vitro cytocompatibility investigation on the designed Mg-Zn-Ag metallic glasses for biomedical application, Journal of Magnesium and Alloys, https://doi.org/10.1016/j.jma.2022.09.025

the tissue healing [4]. Then, more attentions have been paid on corrosion mode and mechanical integrity during the developing of biodegradable Mg alloys [5]. The Mg-based alloys such as Mg-Zn [6,7], Mg-Ag [8], Mg-Cu [9–11], Mg-Zn-Sr [12–14], Mg-Zn-Ca [7,15] and Mg-Ag-Cu [16,17] have been widely studied, but the improvement is limited. The recent research [18] on different Zn doped Mg-Gd alloy reveals that the appropriate content of stacking fault or precipitates with uniform distribution could benefit the corrosion resistance and mechanical integrity simultaneously. While the study on Mg with Ca micro-alloying exhibits excellent corrosion resistance, which is attributed to inhibition of cathodic water reduction kinetics, impurities stabilizing and a protective surface film [19]. For Mg alloys, the increasing of mechanical properties always need more alloying elements, which is detrimental to the corrosion resistance. Therefore, it is still a problem to balance the mechanical properties and corrosion behavior of the Mg alloys for biomedical application.

According to the previous research, the presence of Mg ion could promote the increase of neuronal calcitonin gene-related polypeptide-α (CGRP) in both the peripheral cortex of the femur and the ipsilateral dorsal root ganglia (DRG), which enhanced magnesium-induced osteogenesis [20]. Then, it can be prospected that the Mg and its alloys could be applied for the therapy of bone osteoporosis or bone tissue repair. However, the controlled biodegradation is a key issue for the Mg alloys before their successful applications. The previous researches [21,22] reveal that the zinc (Zn) element plays plentiful biological functions in the human body, which also can enhance the corrosion resistance and mechanical property of Mg alloys. In addition, the bacterial infection always happens during the surgical operation. If the implant could have the antibacterial function, it would benefit the postoperative healing. Actually, the metal ion Argentum^{+} (Ag+) has excellent antibacterial properties and been conventionally used as an antibacterial agent [23,24]. Moreover, the Ag could play an essential role to increase the pitting corrosion resistance of Mg alloys [25]. Recently, Mg-based alloys containing Zn and Ag elements have been studied which demonstrates well improved corrosion resistance [26,27]. However, the degradation behavior of the Ag and Zn doped Mg alloys are still not satisfied for the bone repair filler, their corrosion rate should be decreased further by more methods [28,29]. Based on the reported results [30–32], the secondary phase, grain boundary and crystal defect in the Mg alloys are detrimental to the corrosion resistance.

The study on the amorphous Mg alloy exhibits that it processes excellent corrosion resistance and homogeneous degradation [33]. Such improvements are ascribed to the relative homogeneous elemental distribution in the amorphous system which eliminates the microstructural defects such as grain boundaries, dislocations and precipitates [21,22]. Therefore, it would be expected to apply the amorphization on the Mg alloys to obtain better biodegradation behavior. However, there is almost no research on the Mg-Zn-Ag metallic glasses. Thus, the study of Mg-Zn-Ag metallic glasses will fill the gap in the development of Mg-based metallic glasses, which could play an important role in the design of ternary Mg-Zn-Ag and quaternary Mg-Zn-Ag-X metallic glasses for biomedical application.

Thus, in the present work, the Mg alloys with different component of Zn were designed by the CALPHAD method, and then fabricated by single-roller melt-spinning. The obtained thin strips were investigated by corrosion test and cell culture to evaluate their corrosion behavior and cytocompatibility. The present research would be helpful to the developing of Mg-based metallic glasses for bone tissue repairing application.

2. Experimental procedure

2.1. Mg-Zn-Ag metallic glasses preparation

Seven samples with nominal composition of $Mg_{96\text{-}x}Zn_xAg_4$ ($x = 17$, 20, 23, 26, 29, 32, 35, at.%) were selected. All samples were prepared using high-purity magnesium (99.9 wt.%), zinc (99.99 wt.%) and silver (99.9 wt.%) purchased from Trillion Metals company, Beijing, China. Before melting, raw metals were ground with 400 grit particle sizes of sandpaper to remove the oxide layer. Graphite crucible was used in the melting process. Mg and Zn were compensated with an extra 0.5 wt.% during the sample weighting due to their high vapor pressure. All samples were melted in an induction furnace under the argon atmosphere at least three times in order to obtain the as-cast ingots with homogeneous microstructure. The weight loss of each sample after the melting process is less than 2 wt.%. After melting, as-cast samples were ground with sandpaper to remove the impurities and oxide layer on the surface. Then, they were cut into small pieces and put into a single port glass tube for single-roller melt-spinning. The diameter of the small opening of the single port glass tube is approximately 1 mm. The distance between the glass tube and the copper roller is controlled at about 2 mm. The single-roller melt-spinning process was carried out under a high purity argon atmosphere with the speed of 1800 n/min, which converts to a wheel tangential speed of about 28.3 m/s.

2.2. Microstructure and phase characterization

The XRD technique was carried out to verify the amorphous state on the free side of each ribbon. The X-ray patterns were obtained by D8 Advance Polycrystalline machine with the 45 kV and 40 mA CuKα radiation. The spectra were acquired from 20° to 90° (2θ) with a 0.1°/s step size. The Jade-6 analysis software was used to analyze the amorphous properties of samples. The DSC measurement was carried out using pure Al_2O_3 crucible under a continuous argon flow to investigate the thermal stability and glass transition of the as-quenched glassy samples. The instrument was calibrated with pure Mg firstly. The baseline was obtained with an empty Al_2O_3 crucible to reduce the systematic error. Each ribbon was tested using the STA499 F3 machine at the heating and cooling rates of 5, 10, 20, and 40 K/min. No reaction was observed between the samples and the Al_2O_3 crucibles after

the test. The surface morphology, elemental composition and distribution of the free side of Mg-Zn-Ag metallic glasses before and after corrosion were characterized by Gemini SEM 300 scanning electron microscopy equipped with an energy-dispersive spectroscope. An accelerating voltage of 10 kV was used to obtain SEM images and perform EDS analysis. The laser scanning confocal microscope (LSCM; KEYENCE VX-X200) were applied to observe original and after removing the corrosion layer morphologies of Mg-Zn-Ag metallic glasses at 50 times of magnification.

2.3. The immersion test

The immersion tests of amorphous ribbons were carried out in simulated body fluid (SBF) to obtain the corrosion rate (CR). The SBF solution was prepared with specific ratio of 8 g/L NaCl, 0.04 g/L KCl, 0.14 g/L $CaCl_2$, 0.35 g/L $NaHCO_3$, 0.1 g/L $MgCl_2$, 0.06 g/L $MgSO_4$, 0.06 g/L KH_2PO_4 and 0.06 g/L $NaHPO_4$. The buffer solution is used with distilled water. Before the immersion test, the pH value of SBF solution was adjusted to 7.4 using NaOH and $NaHCO_3$. The immersion test was performed by soaking the ribbon samples in SBF solution at room temperature, where the ratio of sample surface and SBF solution volume was 1.25 cm^2/ml. The SBF solution was replaced in every 24 h. All samples were washed and dried with deionized water after soaking for 3, 7, and 14 days. The corrosion products on the surface of each sample were removed in a chromic acid solution of 200 g/L CrO_3 and 10 g/L $AgNO_3$ according to the ASTM G1–03 standard. The corrosion rate (CR, mm/year) of the samples in SBF solution can be calculated according to the following equation: $CR = (K \times W)/(A \times T \times \rho)$, where the constant value K is 8.76×10^4; W is the mass loss in gram; A is the contact area in cm^2; T is the soaking time in hour; ρ is the density in $g \cdot cm^3$. The volume and mass of Mg-Zn-Ag metallic glasses were obtained by drainage method and electronic balance, respectively. The density of Mg-Zn-Ag metallic glasses is calculated by the ratio of mass to volume.

The optima 7300 DV inductively coupled plasma spectrometer (ICP) produced by PerkinElmer Company of United States was employed for ion concentration test of corrosion solutions. The pH value of the SBF solution was also monitored during the immersion periods. The SBF solution without any sample was used as a control group.

2.4. In vitro cell experiment

The cell morphology in direct contact and indirect contact with biological cells were obtained using a cell morphology observation experiment. The aseptic alloy samples were immersed into the 24-well medium containing 2×10^5 cells for the direct contact culture test. Each well contains 1 ml medium and 5 mg amorphous ribbons. The cells were cultured at 37 °C with 5% CO_2 incubator. The indirect contact culture was carried out based on the results obtained from the direct contact culture. Add 400 μl supernatant to 400 μl medium containing 2×10^5 MDCK cells or RD cells for the indicated time. The cell morphology was examined by an optical microscope (BDS 400) at each selected time. The aseptic treatment of alloy samples included ultrasonic cleaning for 10 min, centrifugation for 10 min and ultraviolet sterilization for 2 h. The biological cells were seeded in the medium without alloy sample as the control group.

The cytotoxicity evaluation was performed by the RD cell, MTT biological reagent, and cell viability detector to evaluate the cell viability of Mg-Zn-Ag metallic glasses. Specifically, 5 mg amorphous ribbons after aseptic treatment were put into 1 ml medium. After 3 days of culture, 400 μl supernatant was extracted. Given the slow degradation rate of degradable metals in the body and the rapid metabolic exchange of degradation products, the supernatant was diluted with fresh medium at 1:1 and 1:2 and put into 96-well plate. Each plate was inoculated with 2×10^6 RD. Three samples were taken for each group, and the average value was obtained. A blank medium containing the same concentration of RD was used as a control group. After being cultured at 37 °C in 5% CO_2 incubator for 2 and 4 days, MTT reagent was added. The 96-well plate was put into the cell viability detector to detect the cell viability.

3. Results and discussions

3.1. Mg-Zn-Ag metallic glasses characterization and thermodynamic calculations

3.1.1. Prediction of glass forming ability (GFA) with thermodynamic calculations

The GFA can be estimated by calculating the driving forces (DFs) of all crystalline phases under the supercooled liquid phase. The calculated DFs of each phase in the Mg-Zn binary system with the increasing of Zn content at the 300 °C are shown in Fig. 1a. Along with the varying of Zn content, the DFs of crystalline compounds show a "U' shape with a minimum value at the composition around 28 at.% Zn. According to the present DFs' criterion, this composition region with minimum DFs is expected to have good GFA of Mg-Zn alloys [34]. Moreover, the present calculations show a good agreement with the previously experimental data [35,36] as shown in Fig. 1a.

Then, in order to find the composition of Mg-Zn-Ag alloys with better GFA, the DFs of crystalline compounds in Mg-Zn-Ag ternary system at 300 °C were calculated with constant value of 4 at.% Ag as shown in Fig. 1b. The "U" shape of compounds' DFs also is appeared in the composition region 19 to 29 at.% Zn for $Mg_{96-x}Zn_xAg_4$ alloys. As shown in Fig. 1b, the composition with super GFA is shifting to Mg-rich region with the addition of Ag. According to the present calculations, the alloys Mg96-xZnxAg4 ($x = 17$, 20, 23, 26, 29, 32, 35, in at.%) with relatively high DFs were selected for the metallic glass preparation.

3.1.2. Mg-Zn-Ag metallic glasses characterization

The XRD patterns of the free side of the $Mg_{96-x}Zn_xAg_4$ ($x = 17$, 20, 23, 26, 29, 32, 35) ribbons obtained by the

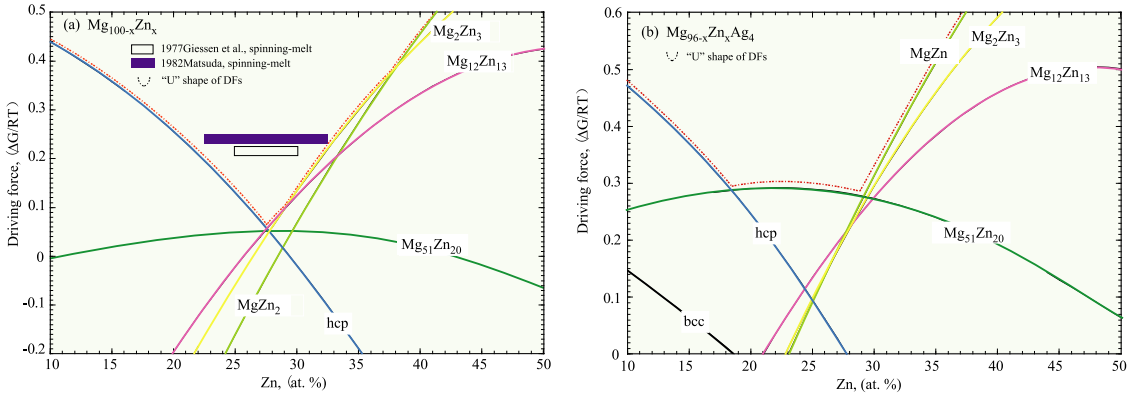

Fig. 1. The calculated DFs of individual crystalline phases of (a) Mg-Zn and (b) $Mg_{96-x}Zn_xAg_4$ alloys using CALPHAD technique.

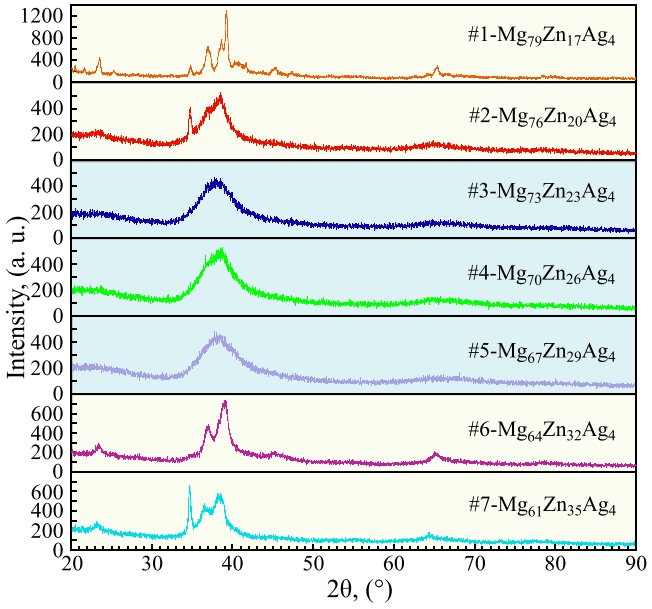

Fig. 2. XRD patterns of #1-$Mg_{79}Zn_{17}Ag_4$, #2-$Mg_{76}Zn_{20}Ag_4$, #3-$Mg_{73}Zn_{23}Ag_4$, #4-$Mg_{70}Zn_{26}Ag_4$, #5-$Mg_{67}Zn_{29}Ag_4$, #6-$Mg_{64}Zn_{32}Ag_4$ and #7-$Mg_{61}Zn_{35}Ag_4$ samples obtained by powder XRD diffraction.

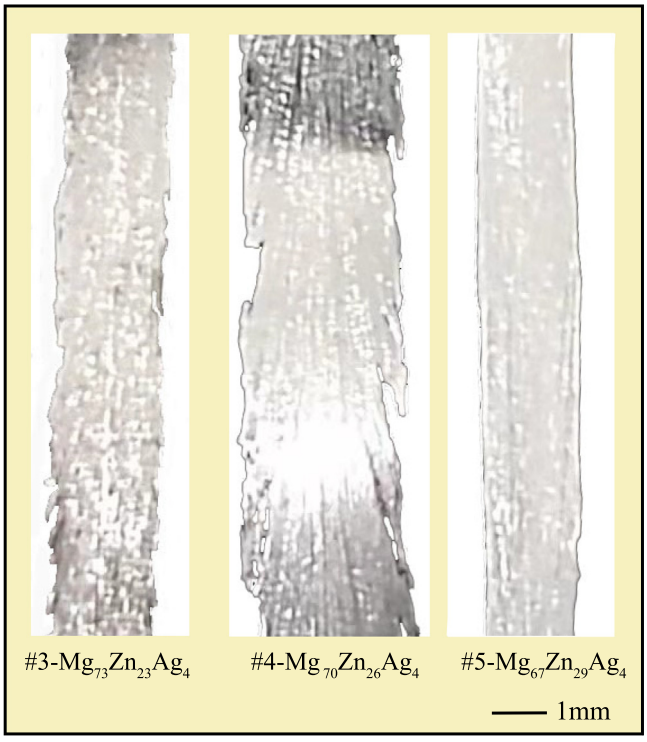

Fig. 3. The images of the Mg–Zn–Ag metallic glasses with the #3-$Mg_{73}Zn_{23}Ag_4$, #4-$Mg_{70}Zn_{26}Ag_4$ and #5-$Mg_{67}Zn_{29}Ag_4$ compositions.

melt-spinning method are shown in Fig. 2. Clearly, with the increase of Zn content, the microstructure of the samples have experienced great evolution which transforms from multi-phase structure to amorphous structure and then multi-phase structure. For the samples #3-$Mg_{73}Zn_{23}Ag_4$, #4-$Mg_{70}Zn_{26}Ag_4$, and #5-$Mg_{67}Zn_{29}Ag_4$, the appearance of wide and strong amorphous characteristic diffraction peaks around 30° to 50° confirms their amorphous nature. Several crystal peaks appeared in the diffraction patterns for the samples #1-$Mg_{79}Zn_{17}Ag_4$, #2-$Mg_{76}Zn_{20}Ag_4$, #6-$Mg_{64}Zn_{32}Ag_4$, and #7-$Mg_{61}Zn_{35}Ag_4$ indicate these alloys constituted with the composite microstructure of amorphous and crystalline phases. Macrographic observations on the samples #3-$Mg_{73}Zn_{23}Ag_4$, #4-$Mg_{70}Zn_{26}Ag_4$, and #5-$Mg_{67}Zn_{29}Ag_4$ demonstrate the width of approximately 2∼3 mm and thickness of 30 μm, as shown in Fig. 3. Comparatively, the sample #4-$Mg_{70}Zn_{26}Ag_4$ has the biggest width and the #5-$Mg_{67}Zn_{29}Ag_4$ has the smallest width, but the sample #5-$Mg_{67}Zn_{29}Ag_4$ has best edge, which indicates its good casting capability.

In order to determine the glass-forming ability (GFA) of Mg-Zn-Ag samples, the glass transition temperature (T_g), melting temperature (T_m), and crystallization temperatures (T_{p1}, T_{p2}, T_{p3}…) of #3-$Mg_{73}Zn_{23}Ag_4$, #4-$Mg_{70}Zn_{26}Ag_4$, and #5-$Mg_{67}Zn_{29}Ag_4$ were measured in the present work. The characteristic temperatures: T_g, T_m, T_{p1}, T_{p2}, and T_{p3} of samples #3-$Mg_{73}Zn_{23}Ag_4$, #4-$Mg_{70}Zn_{26}Ag_4$, and #5-$Mg_{67}Zn_{29}Ag_4$ were determined using DSC measurements with heating rate of 5, 10, 20, and 40 K/min are shown in Fig. 4 and summarized in Table 1. The glass transition temperature (T_g), crystallization temperatures (T_{p1}, T_{p2}, T_{p3}…) increase monotonically with decreasing Mg content.

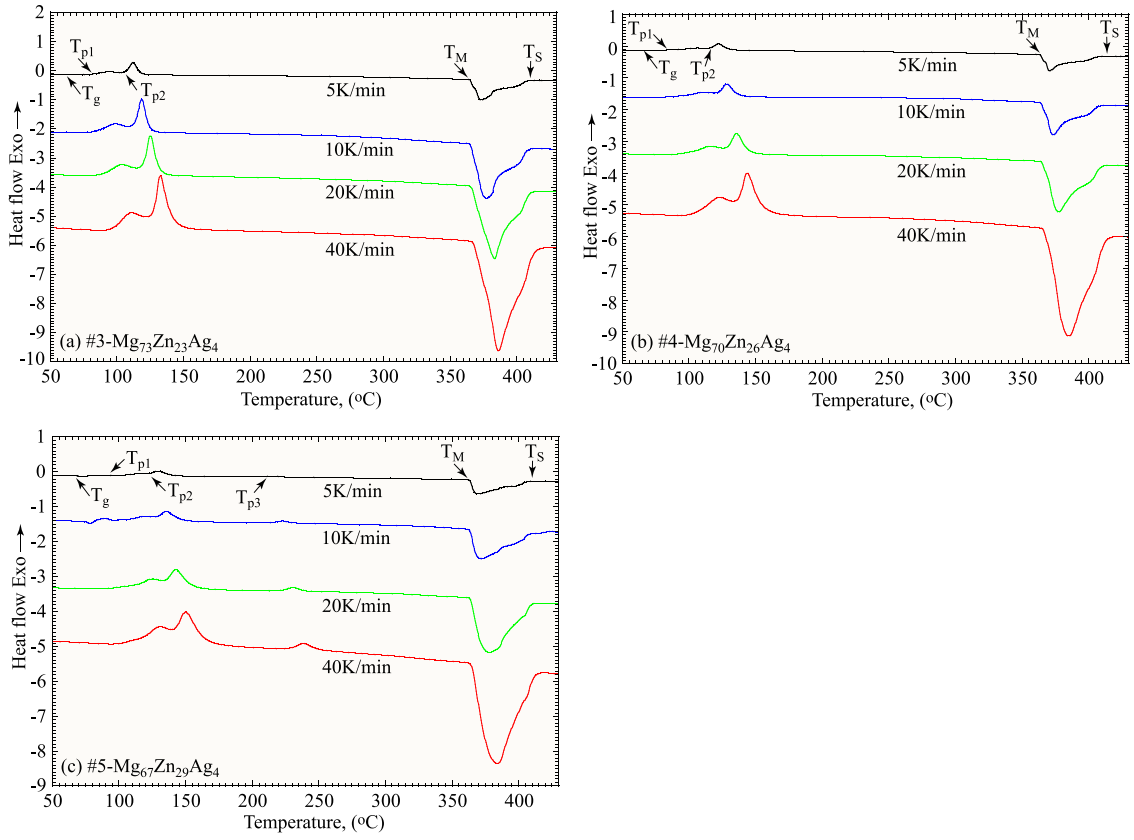

Fig. 4. The DSC curves of the Mg–Zn–Ag metallic glasses at 5, 10, 20 and 40 K/min heating rates: (a) #3-$Mg_{73}Zn_{23}Ag_4$, (b) #4-$Mg_{70}Zn_{26}Ag_4$ and (c) #5-$Mg_{67}Zn_{29}Ag_4$.

Table 1
Characteristic temperatures and activation energies for crystallization of $Mg_{96-x}Zn_xAg_4$ ($x = 23, 26, 29$) metallic glasses.

Sample	Crystallization temperature (K)	Heating rate (K/min)				Activation energy (kJ/mol)		T_{rg} (T_g/T_s)
		5	10	20	40			
#3-$Mg_{73}Zn_{23}Ag_4$	T_{p1}	350.9	354.3	359.4	365.6	E_{p1}	204.9	0.507
	T_{p2}	378.4	382.5	389.1	395.6	E_{p2}	197.1	
#4-$Mg_{70}Zn_{26}Ag_4$	T_{p1}	354.7	358.1	363.4	372.8	E_{p1}	209.4	0.508
	T_{p2}	389.2	393.6	400.8	407.8	E_{p2}	194.1	
#5-$Mg_{67}Zn_{29}Ag_4$	T_{p1}	370.4	374.2	379.3	385.1	E_{p1}	204.0	0.525
	T_{p2}	396.0	400.6	407.1	413.8	E_{p2}	192.1	
	T_{p3}	481.1	488.1	495.1	501.2	E_{p3}	201.4	

*Note: T_{p1} and T_{p2} are crystallization peak temperatures, E_{p1} and E_{p2} are activation energies.

The characteristic temperatures shift to higher with increasing heating rate, as shown in Fig. 4 and listed in Table 1. The dependence of the heating rate of phase crystallization in metallic glasses indicates that the nucleation and phase transition with a heating rate of 0 K/min can be extrapolated linearly with the values from 5, 10, 20, and 40 K/min by thermal activation process, while the rate of kinetic glass transition temperature (T_g) depends on the relaxation process of glass transition zone. The apparent activation energy of each characteristic transformation was evaluated by Kissinger method [37], as shown in Table 1. The higher the apparent activation energy related to the higher the anti-crystallinity tendency, where the better GFA can be obtained. The maximum E_p obtained from sample #5-$Mg_{67}Zn_{29}Ag_4$ indicates the best thermal stability of metallic glasses compared to other samples. The composition dependence of the reduced glass transition temperature ($T_{rg} = T_g/T_s$) with compositions for the Mg-Zn-Ag metallic glasses, as listed in Table 1. The ''strong liquid'' behavior of metallic glasses results in a reduced rate of both crystal nucleation and growth, and therefore contributes greatly to the extraordinary GFA [38]. The maximum T_{rg} was found to be 0.525 at a composition close to $Mg_{67}Zn_{29}Ag_4$, resulting in the best GFA.

3.2. Corrosion behavior investigation

The density of Mg-Zn-Ag metallic glasses and their corrosion rates after immersion in SBF solution for 3, 7, and 14 days are listed in Table 2. The density of Mg-Zn-Ag metallic glasses increases with the increase of Zn content in the

Table 2
The Density of Mg-Zn-Ag metallic glasses and their corrosion rates after immersion in SBF solution for 3, 7, and 14 days.

Sample	Density, ρ (g/cm^3)	Corrosion rate, 3d (mm/year)	Corrosion rate, 7d (mm/year)	Corrosion rate, 14d (mm/year)
#3-$Mg_{73}Zn_{23}Ag_4$	3.38	0.38±0.03	0.34±0.03	0.31±0.01
#4-$Mg_{70}Zn_{26}Ag_4$	3.45	0.34±0.02	0.32±0.01	0.30±0.02
#5-$Mg_{67}Zn_{29}Ag_4$	3.56	0.22±0.03	0.21±0.02	0.19±0.02

Table 3
The element components of products on surface of samples obtained by EDS after mmersion with 3, 7 and 14 days.

Elememt (at.%)	O	Na	Mg	P	Cl	Ca	Zn	Ag
#3-$Mg_{73}Zn_{23}Ag_4$–3d	35.70	2.91	37.25	3.36	0.12	4.00	13.79	2.87
#4-$Mg_{70}Zn_{26}Ag_4$–3d	56.72	2.42	16.85	7.67	0.47	9.56	5.23	1.08
#5-$Mg_{67}Zn_{29}Ag_4$–3d	57.51	5.64	12.13	5.13	0.55	5.86	11.18	1.99
#3-$Mg_{73}Zn_{23}Ag_4$–7d	60.57	1.46	13.49	8.16	0.70	9.88	4.39	1.35
#4-$Mg_{70}Zn_{26}Ag_4$–7d	53.67	2.44	17.98	6.90	0.11	7.19	9.70	2.01
#5-$Mg_{67}Zn_{29}Ag_4$–7d	45.79	2.75	24.91	6.37	0.17	6.95	11.03	2.03
#3-$Mg_{73}Zn_{23}Ag_4$–14d	50.10	1.99	22.72	6.77	0.09	7.37	8.76	2.20
#4-$Mg_{70}Zn_{26}Ag_4$–14d	42.04	2.52	30.80	4.43	0.12	4.48	13.08	2.53
#5-$Mg_{67}Zn_{29}Ag_4$–14d	46.30	3.29	22.00	5.43	0.18	5.74	14.48	2.58

nominal composition. While the corrosion rates of Mg-Zn-Ag metallic glasses after immersion in SBF solution for 3, 7, and 14 days decrease with the increase of Zn content. Although the metallic glass could be treated with a homogenous microstructure, but the different kind of local atomic clusters would existed in the matrix [39]. The increased Zn addition would promote the formation of atomic clusters with high Zn content, which could play the role of "region protective shield", because of the relative high potential of Zn. This may be the main reason that results in the corrosion rate changing tendency of Mg-Zn-Ag metallic glasses with the increasing of Zn. Furthermore, the corrosion rates of Mg-Zn-Ag metallic glasses decrease as the days of immersion in SBF solution increase, which should be ascribed to the formed corrosion product with relative homogeneous distribution and forming barrier layer between the simulated body fluid and metallic glasses. The corrosion rates change of sample #3-$Mg_{73}Zn_{23}Ag_4$ is the most significant with immersion time. According to the recent research [40], the corrosion rate should be less than 0.5 mm/year for the biodegradable materials used as implant to meet the requirement of the tissue repair. In the present research, the Mg-Zn-Ag based metallic glasses have lower corrosion rate than the suggested value. Moreover, the declined corrosion rates with the time would be more suitable with the tissue repairing process.

The SEM characterizations on Mg-Zn-Ag metallic glasses before and after immersion in SBF solution for 3, 7, and 14 days are shown in Fig. 5. The element components of products on surface of samples obtained by EDS after immersion with 3, 7 and 14 days are listed Table 3. The SEM observations on the ribbon surface of samples #3-$Mg_{73}Zn_{23}Ag_4$, #4-$Mg_{70}Zn_{26}Ag_4$, and #5-$Mg_{67}Zn_{29}Ag_4$ before immersion demonstrate the obvious pit defects (see Fig. 5a-c). The pits demonstrate clear elongated morphology along the spinning direction. However, the size and quantity of the pit defect decreases with the increased Zn content. Actually, the pits will affect the contact area during the immersing test, which would result in slightly increased actual surface area than the nominal area in immersion tests. However, the experimental error limit is still within the acceptable range. After the 3, 7, and 14 days of immersion, surface of Mg-Zn-Ag metallic glasses exhibits typical corroded features of covered film embellished with small particles. Small cracks generate on the surface of the samples immersed for 3, 7, and 14 days, which mainly resulted from the dehydration of the corroded product film. Such a phenomenon indicates the relative compact film is formed on the surface, which is beneficial to the corrosion resistance. Compared with the three metallic glasses samples, the cracks in the #3-$Mg_{73}Zn_{23}Ag_4$ are bigger and denser, while the cracks in the #4-$Mg_{70}Zn_{26}Ag_4$ are smaller and fewer. Based on the surface features, it can be deduced that the corroded product films on the three kinds of metallic glasses samples almost maintain integral. When the immersion time extends to 14 days, the surfaces of the metallic glasses evolve differently.

To further study the corroded product film, the elemental distribution of Mg-Zn-Ag metallic glasses immersed in SBF solution for 3 days has been analyzed by EDS, as shown in Figs. 6-8. The different matrix composition has resulted in the different surface corroded product and morphology. For the #3-$Mg_{73}Zn_{23}Ag_4$ sample as example, its typical elemental distribution analysis reveal that the aggregated particles are rich of Ca, P and O, as shown in Fig. 6. According to the previous research [41,42], the simultaneous presence of Ca, O, and P indicates the formation of apatite. While the rest area is rich of Mg, Zn and O, which means the $Mg(OH)_2$ and $(Zn(OH)_2$ should be the main corroded product. Moreover, it seems that the Zn prefers to segregate along the cracks. It can be deduced from these phenomena that the relative rapid reaction of Mg matrix with the SBF promotes the formation of the apatite [43]. Due to the better corrosion resistance, the Zn would like to segregate along the boundary of the corroded film to balance its whole corrosion properties. However, the MgO and ZnO formed after the dehydration have obvious dif-

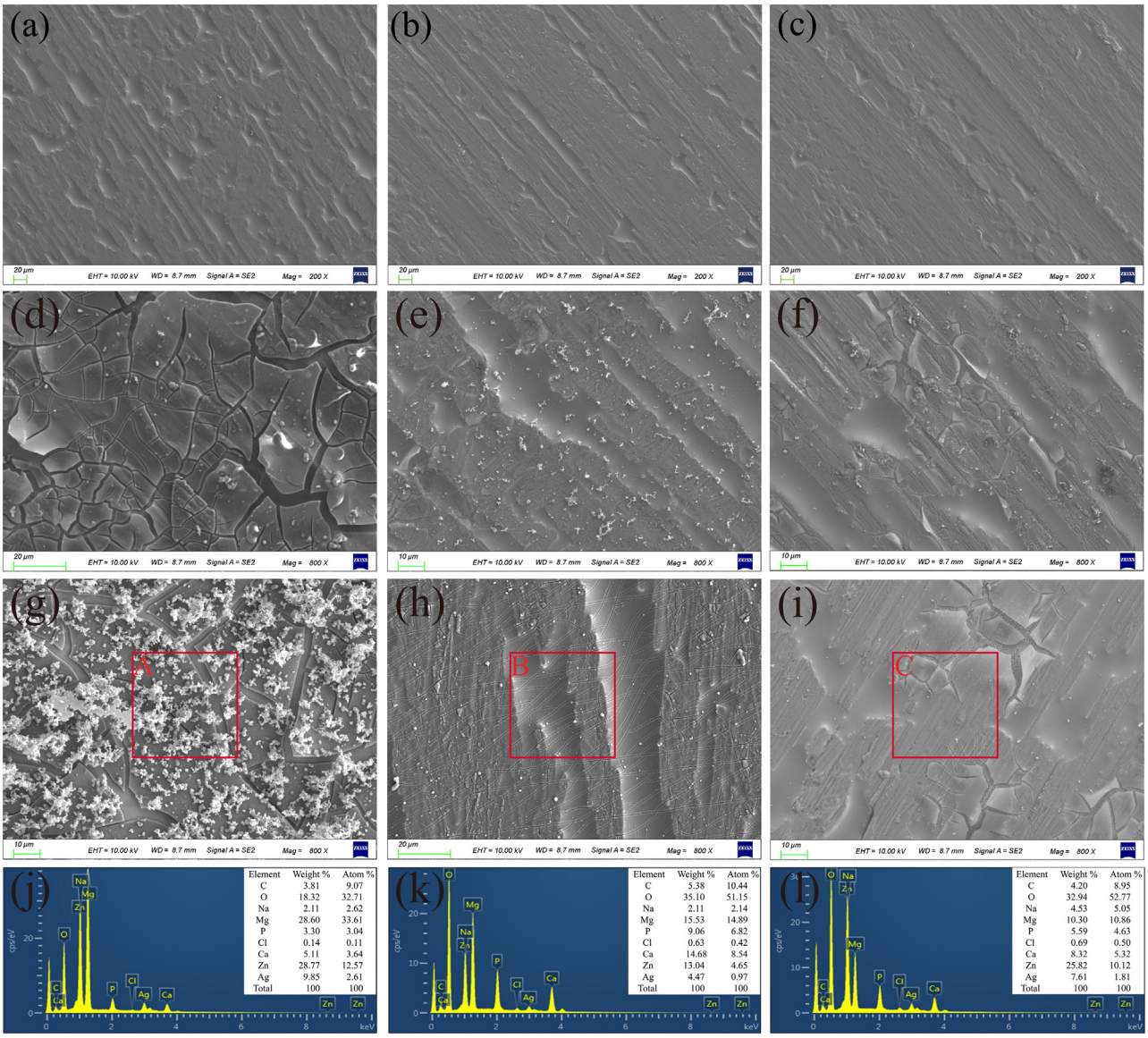

Fig. 5. Surface morphology observations with SEM on Mg–Zn–Ag metallic glasses before and after immersion in SBF solution: (a) #3-$Mg_{73}Zn_{23}Ag_4$, (b) #4-$Mg_{70}Zn_{26}Ag_4$ and (c) #5-$Mg_{67}Zn_{29}Ag_4$ before immersion; (d) #3-$Mg_{73}Zn_{23}Ag_4$, (e) #4-$Mg_{70}Zn_{26}Ag_4$ and (f) #5-$Mg_{67}Zn_{29}Ag_4$ after immersion for 3 days; (g) #3-$Mg_{73}Zn_{23}Ag_4$, (h) #4-$Mg_{70}Zn_{26}Ag_4$ and (i) #5-$Mg_{67}Zn_{29}Ag_4$ after immersion for 7 days; (j) #3-$Mg_{73}Zn_{23}Ag_4$, (k) #4-$Mg_{70}Zn_{26}Ag_4$ and (l) #5-$Mg_{67}Zn_{29}Ag_4$ after immersion for 14 days; The inset in images shows the EDS spectra of the corrosion products after immersion on samples' surface.

ference in crystal structure, which could generate great stress and result in the cracks.

As for the #4-$Mg_{70}Zn_{26}Ag_4$ sample, its typical elemental distribution analysis reveals that the elements distribute homogeneously in most area, except the cracks, as shown in Fig. 7. Along the cracks, the Zn and Mg segregate obviously, but lacking of Ca, O and P. Such a feature is similar with the #3-$Mg_{73}Zn_{23}Ag_4$ sample, but the amount of apatite decreases obviously. For the #5-$Mg_{67}Zn_{29}Ag_4$ sample, its typical elemental distribution analysis shows really homogeneous characteristics, as shown in Fig. 8. The features of the #4-$Mg_{70}Zn_{26}Ag_4$ and #5-$Mg_{67}Zn_{29}Ag_4$ samples verify their good corrosion resistance, due to the integrated and compact surface film.

In order to reveal the corrosion behavior of the Mg-Zn-Ag metallic glasses, the corrosion products were removed and the corroded surface was observed, as shown in Fig. 9. For the #3-$Mg_{73}Zn_{23}Ag_4$ sample immersed in SBF solution for 3 days, small pits and large corrosion areas are the main characteristics, as shown in Fig. 9a. The strip protrusions (see Fig. 9d) and more corrosion pits appeared uniformly (see Fig. 9g) with the increasing of immersion time. The size distributes from hundreds of nanometers to several microns. In addition, the pits distribute in most area, but there are still some isolated region with smaller pits. For the #4-$Mg_{70}Zn_{26}Ag_4$ sample, the ultrafine pits with hundreds of nanometers are the main feature embellished small pits with several microns, as shown in Fig. 9b. With the increasing

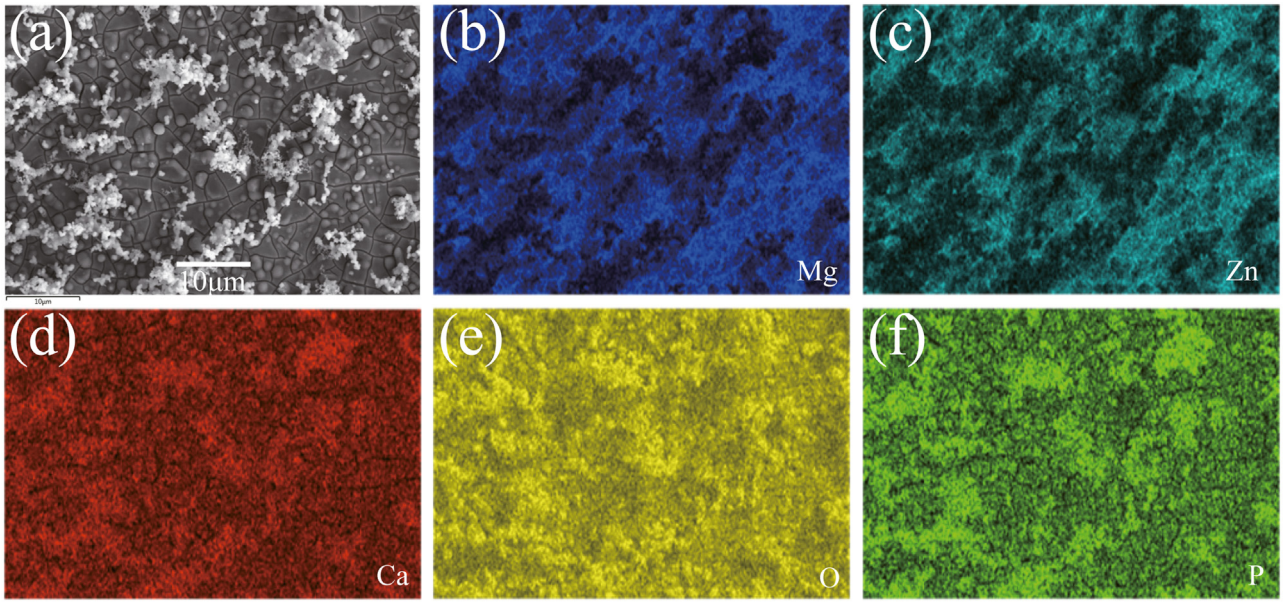

Fig. 6. SEM image of corroded surface of #3-$Mg_{73}Zn_{23}Ag_4$ sample immersed in SBF solution for (a) 3 days, and its elemental distribution maps of (b) Mg, (c) Zn, (d) Ca, (e) O and (f) P.

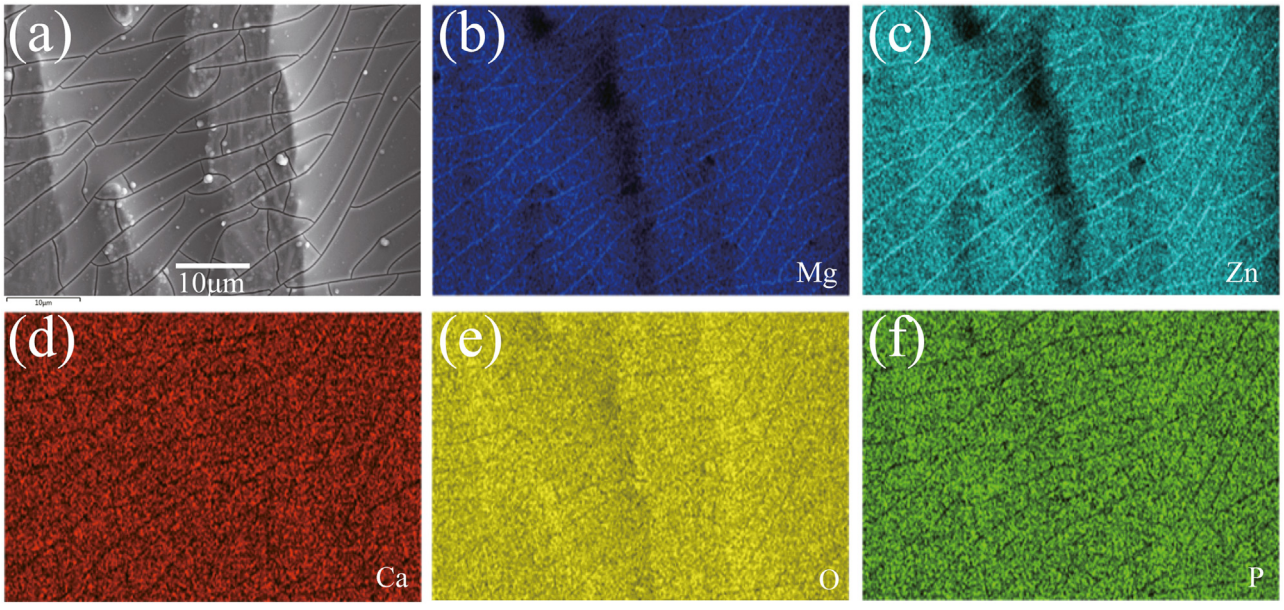

Fig. 7. SEM image of corroded surface of #4-$Mg_{70}Zn_{26}Ag_4$ sample immersed in SBF solution for (a) 3 days, and its elemental distribution maps of (b) Mg, (c) Zn, (d) Ca, (e) O and (f) P.

of immersion time, the change of corrosion surface of #4-$Mg_{70}Zn_{26}Ag_4$ sample is similar to that of #3-$Mg_{73}Zn_{23}Ag_4$ sample. Because of the corrosion rate is less than that of #3-$Mg_{73}Zn_{23}Ag_4$ sample, the corrosion pits have not appeared uniformly on the #4-$Mg_{70}Zn_{26}Ag_4$ sample immersed in SBF solution for 14 days (see Fig. 9h). For the #5-$Mg_{67}Zn_{29}Ag_4$ sample, its pits feature is almost similar with that of the #4-$Mg_{70}Zn_{26}Ag_4$ sample, but the sizes of the pits are smaller, as shown in Fig. 9c. For the #5-$Mg_{67}Zn_{29}Ag_4$ sample immersed in SBF solution for 14 days, the quantity of corrosion pits is lower than that of #3-$Mg_{73}Zn_{23}Ag_4$ and #4-$Mg_{70}Zn_{26}Ag_4$ samples, as shown in Fig. 9i. From the surface morphology observation, the corrosion degree of #5-$Mg_{67}Zn_{29}Ag_4$ sample is less than #3-$Mg_{73}Zn_{23}Ag_4$ and #4-$Mg_{70}Zn_{26}Ag_4$ samples. This phenomena confirms the corroded surface morphology of these samples. The relative rapid corrosion rate may result in the surface film with porous structure, which is apt to cause the cracks during the dehydration. The lower corrosion rate could promotes the more densified surface film. Therefore, the #4-$Mg_{70}Zn_{26}Ag_4$ and #5-$Mg_{67}Zn_{29}Ag_4$ samples have the lower corrosion rate, compared with the #3-$Mg_{73}Zn_{23}Ag_4$ sample.

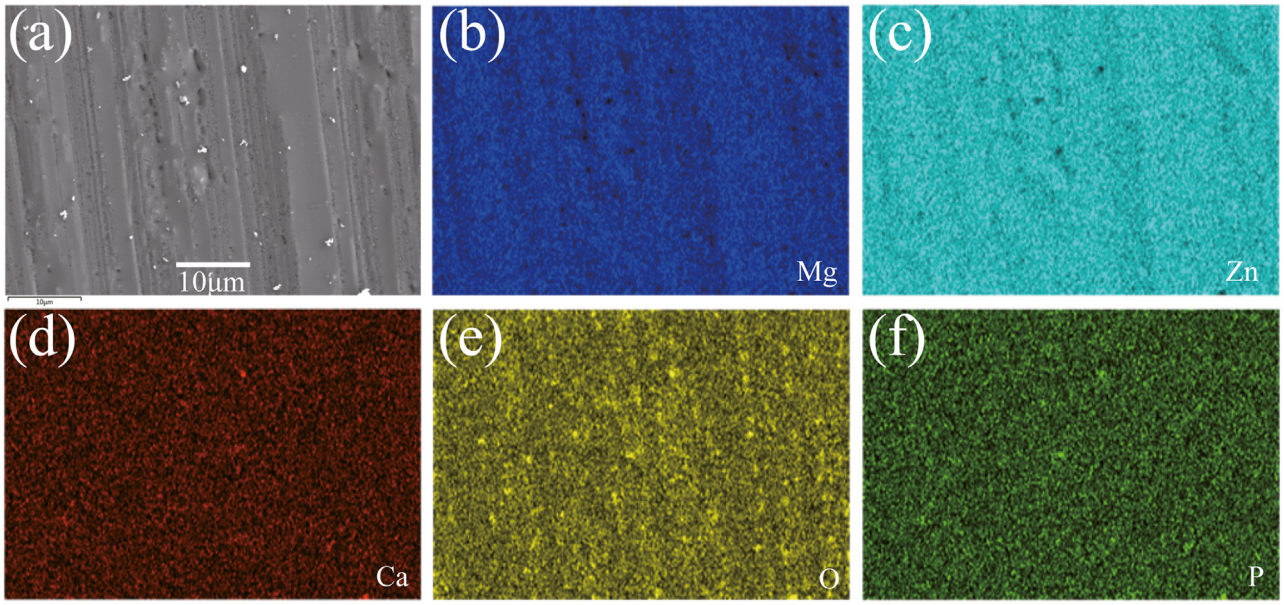

Fig. 8. SEM image of corroded surface of #5-$Mg_{67}Zn_{29}Ag_4$ sample immersed in SBF solution for (a) 3 days, and its elemental distribution maps of (b) Mg, (c) Zn, (d) Ca, (e) O and (f) P.

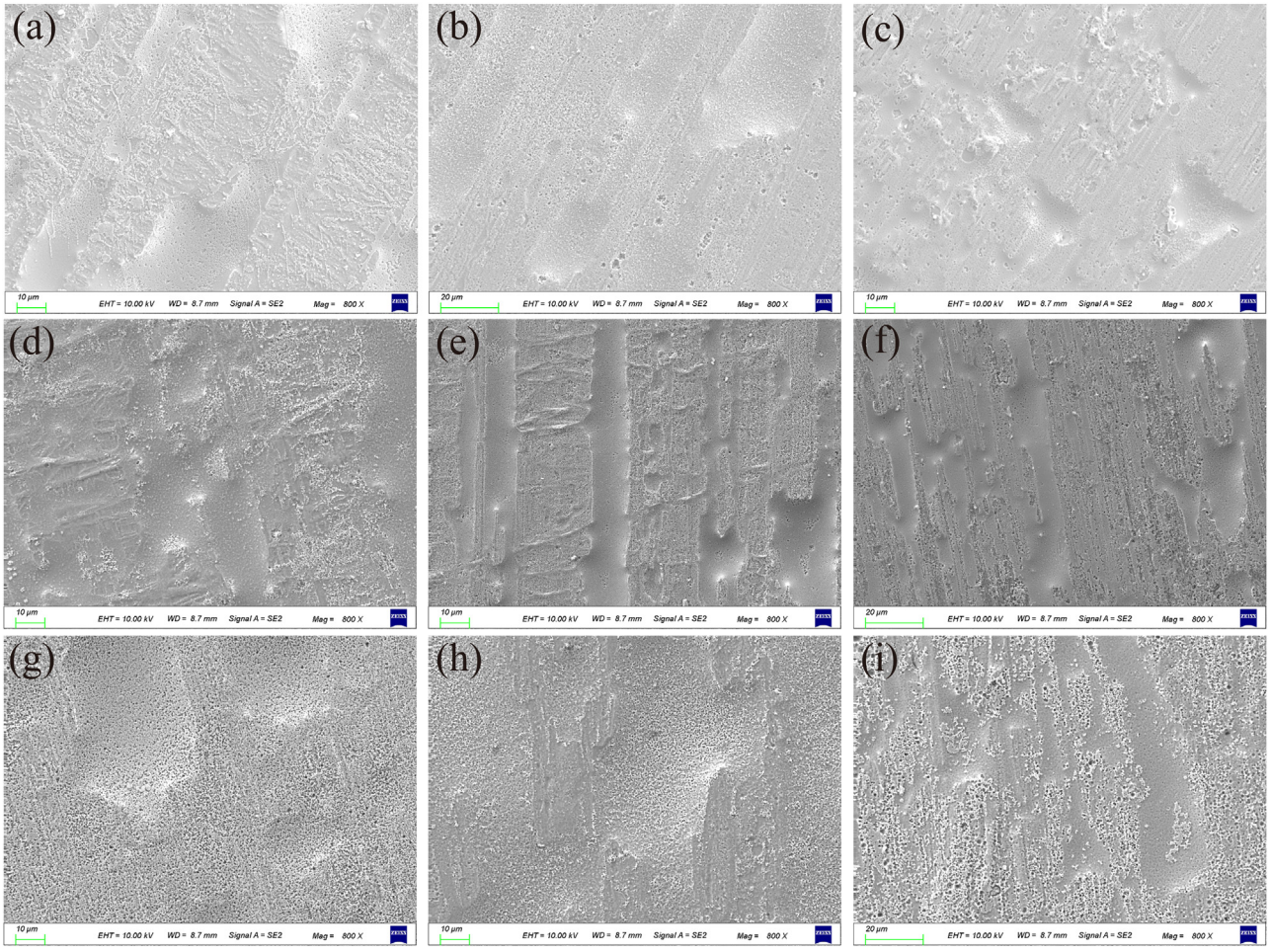

Fig. 9. Surface morphology observations using SEM on Mg–Zn–Ag metallic glasses immersed in SBF solution for 3, 7 and 14 days and cleaned by CrO_3/$AgNO_3$ solution: (a) #3-$Mg_{73}Zn_{23}Ag_4$, (b) #4-$Mg_{70}Zn_{26}Ag_4$ and (c) #5-$Mg_{67}Zn_{29}Ag_4$ immersion for 3 days; (d) #3-$Mg_{73}Zn_{23}Ag_4$, (e) #4-$Mg_{70}Zn_{26}Ag_4$ and (f) #5-$Mg_{67}Zn_{29}Ag_4$ immersion for 7 days; (g) #3-$Mg_{73}Zn_{23}Ag_4$, (h) #4-$Mg_{70}Zn_{26}Ag_4$ and (i) #5-$Mg_{67}Zn_{29}Ag_4$ immersion for 14 days.

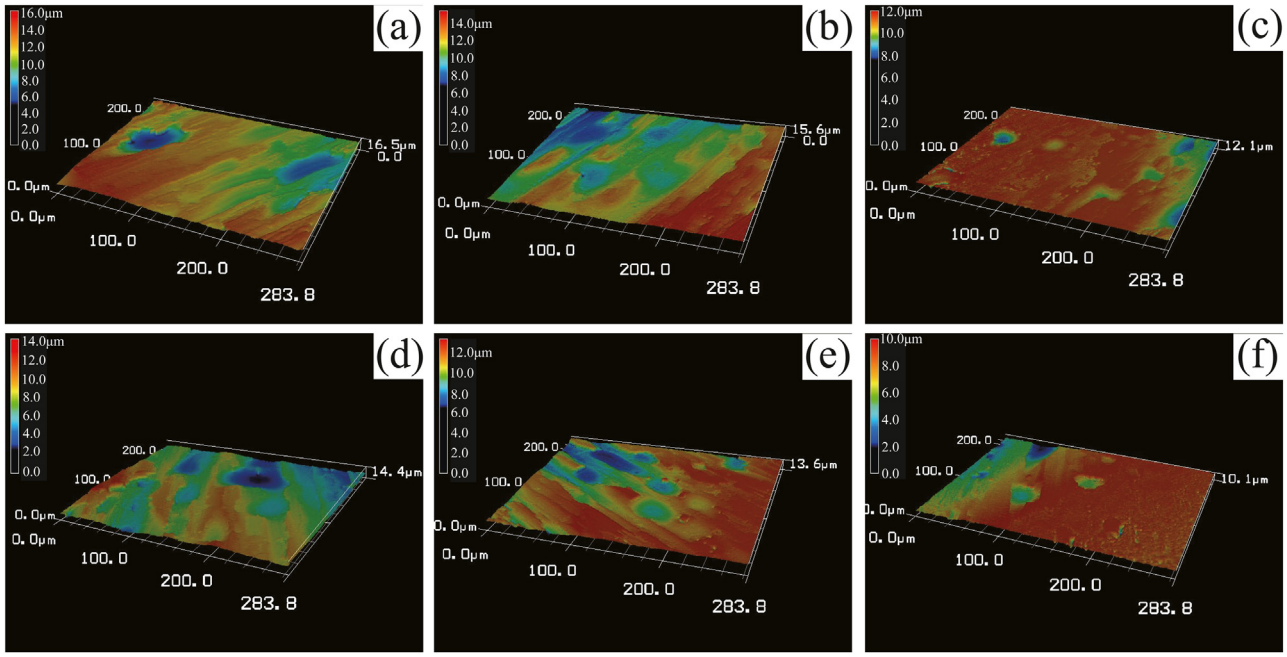

Fig. 10. Three-dimensional reconstruction of LSCM for Mg-Zn-Ag metallic glasses before immersion: (a) #3-$Mg_{73}Zn_{23}Ag_4$ (b) #4-$Mg_{70}Zn_{26}Ag_4$ (c) #5-$Mg_{67}Zn_{29}Ag_4$. Three-dimensional reconstruction of LSCM for Mg-Zn-Ag metallic glasses immersed in SBF solution for 3 days and cleaned by CrO_3/$AgNO_3$ solution: (d) #3-$Mg_{73}Zn_{23}Ag_4$ (e) #4-$Mg_{70}Zn_{26}Ag_4$ (f) #5-$Mg_{67}Zn_{29}Ag_4$.

To comparatively investigate the Mg-Zn-Ag metallic glasses surface evolution after corrosion, the three-dimensional macro-graphic observations on original and corroded surfaces of the samples #3- #5 are shown in Fig. 10. The corroded surfaces are chosen from the specimens immersed in SBF solution for 3 days with removed the surface corrosion products. Obviously can be seen, the average depth of the pit defects of sample #3-$Mg_{73}Zn_{23}Ag_4$ before immersion is the highest among all samples with the value of $6 \pm 0.5\,\mu m$. The pit defects on the surface of samples #3-$Mg_{73}Zn_{23}Ag_4$ tend to deepen after the surface corrosion layer removed. The morphologies of samples #4-$Mg_{70}Zn_{26}Ag_4$ and #5-$Mg_{67}Zn_{29}Ag_4$ after removing the corrosion layer are similar to that before immersion. This is related to the lower corrosion rate of samples #4-$Mg_{70}Zn_{26}Ag_4$ and #5-$Mg_{67}Zn_{29}Ag_4$. The corrosion pits of all samples showed a certain uniformity, without large corrosion pits. It can be concluded that such morphology would be beneficial to the homogeneous degradation.

To evaluate the effect of Mg-Zn-Ag metallic glasses during their degradation, the Mg ion concentrations after their immersion in SBF solution for 1, 3, 5, and 10 days were tested and the results are shown in Fig. 11. Obviously, the Mg ion concentrations are almost increased with the time linearly. The Mg ion concentrations of SBF solutions immersed with #3-$Mg_{73}Zn_{23}Ag_4$, #4-$Mg_{70}Zn_{26}Ag_4$ and #5-$Mg_{67}Zn_{29}Ag_4$ samples for 1 day are 48.67 mg/L, 47.87 mg/L and 34.88 mg/L, respectively. When the immersion time increases to 3 days, the corresponding Mg ion concentrations of SBF solutions increase to 206.3 mg/L, 199.6 mg/L and 166.4 mg/L, respectively. Comparatively, the SBF solution immersed with #3-

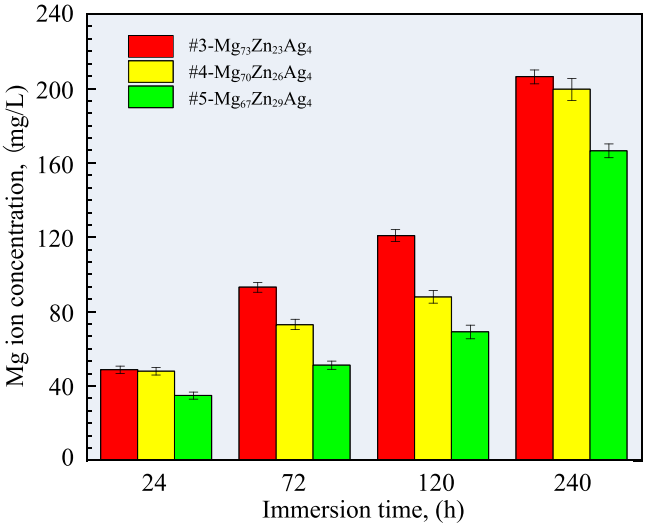

Fig. 11. Mg ion concentrations of the SBF solution with immersed Mg-Zn-Ag metallic glasses for different time.

$Mg_{73}Zn_{23}Ag_4$ sample has the highest Mg ion concentration, while that with #5-$Mg_{67}Zn_{29}Ag_4$ sample has the lowest Mg ion concentration. Based on the corrosion rate and corroded surface, it can be concluded that the releasing of Mg ion during the degradation of Mg-Zn-Ag metallic glasses is depended on their corrosion rates which are related with the chemical composition. Then, the increased Zn content in the Mg-Zn-Ag metallic glasses contribute to the corrosion resistance. Furthermore, the Zn and Ag ion concentrations have not been detected in the SBF solutions with immersion of Mg-Zn-Ag metallic glasses till 10 days, which could be partly ascribed to

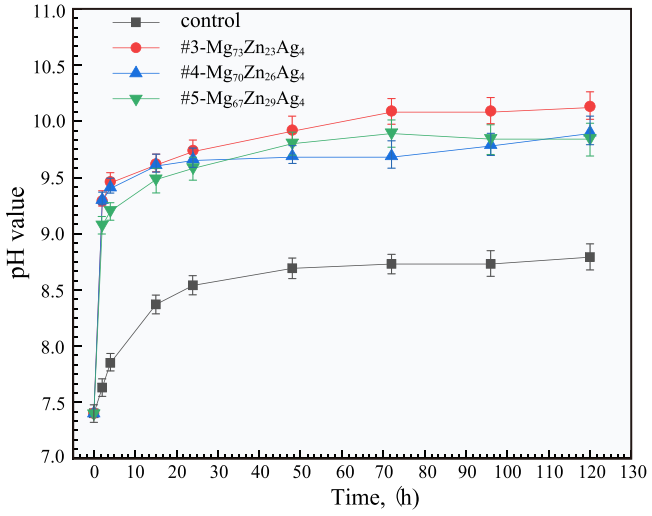

Fig. 12. The pH variation of the SBF solution with immersed Mg-Zn-Ag metallic glasses for different time.

their low content. The elemental distribution maps (Figs. 6–8) showed higher Zn content on the corroded surface during the 3 days immersion period. Similarly, Gu [44] showed that the presence of zinc (oxide/hydroxide) is higher than magnesium (oxide/hydroxide) in the $Mg_{66}Zn_{30}Ca_4$ and $Mg_{70}Zn_{25}Ca_5$ alloys during the initial soaking time of 3 days. In addition, the formation of Zn and Ag atoms clusters would also contribute to the less ion concentration, due to their higher electrode potential [3].

Actually, the degradation of Mg base alloy would result in the ion releasing and pH value variation, which influences the cell activity. Therefore, the pH values of the SBF solution immersed with Mg-Zn-Ag metallic glasses were tested and given in Fig. 12. The SBF solution is set as the control group, which helps to analyze the variation of pH value caused by the degradation of metallic glass samples. It can be seen that the pH values of all SBF solutions immersed with different samples increase greatly in short time and then increase gradually with the time extending. When the immersion time exceeds 70 h, the pH values of all SBF solutions tends to fluctuate between 9.7 and 10.1. Comparatively, the SBF solution immersed with #3-$Mg_{73}Zn_{23}Ag_4$ sample has the highest pH value, while the SBF solution immersed with #4-$Mg_{70}Zn_{26}Ag_4$ and #5-$Mg_{67}Zn_{29}Ag_4$ samples have the lower pH value. Such results are consistent with the corrosion behavior of these Mg-Zn-Ag metallic glasses samples. It should be noted that the SBF solution has a natural increased pH value with the time, which may be caused by the ambient CO_2 gas [45,46]. Consideration of the pH value variation of SBF solution, the pH value of the SBF solution immersed with different Mg-Zn-Ag metallic glasses samples should be lower, which is beneficial to their biocompatibility.

3.3. Cytotoxicity analysis

The direct and indirect culturing of MDCK cells and RD cells were performed to investigate the cytocompatibility or tumor cell inhibitory effect of the Mg-Zn-Ag metallic glasses. The morphology of the MDCK cells directly cultured with different Mg-Zn-Ag metallic glass samples is shown in Fig. 13. Compared with the control group, the MDCK cells cultured on #4-$Mg_{70}Zn_{26}Ag_4$ sample exhibit decreased activity, and those on #3-$Mg_{73}Zn_{23}Ag_4$ and #5-$Mg_{67}Zn_{29}Ag_4$ samples show the similar morphology after 3 days culturing. When the culturing time extends to 7 days, the MDCK cells of the control group proliferate obviously, compared with those cultured for 3 days. While the MDCK cells on #5-$Mg_{67}Zn_{29}Ag_4$ sample just proliferate a little after the culturing for 7 days. The MDCK cells on samples #4-$Mg_{70}Zn_{26}Ag_4$ sample almost lose their luster feature after the culturing for 7 days, which indicates the potential toxicity. When the culturing time extends to 14 days, the MDCK cells on #3-$Mg_{73}Zn_{23}Ag_4$ sample returns to normal, while the MDCK cells on #4-$Mg_{70}Zn_{26}Ag_4$ sample died. The MDCK cells on the #5-$Mg_{67}Zn_{29}Ag_4$ sample exhibit normal morphology, which indicates their higher activities. Such a result may be ascribed to the accumulation of metal ions releasing. These results are almost consistent with the results of immersion test, which indicates the well-controlled corrosion rate could decrease the cyctotoxicity of Mg-Zn-Ag metallic glasses.

To further verify such an opinion, the morphology of the MDCK cells cultured in Mg-Zn-Ag metallic glasses extraction medium was observed, as shown in Fig. 14. Clearly, the MDCK cells cultured in all Mg-Zn-Ag metallic glasses extraction mediums demonstrate the similar state with those in the control group, which indicates the extraction of Mg-Zn-Ag metallic glasses has low cytotoxicity. Then, it can be deduced that the morphology of directly cultured MDCK cells could be attributed to the aggregated Ag in the corroded product film [47]. Actually, the improved corrosion resistance of #5-$Mg_{67}Zn_{29}Ag_4$ sample also restrains the dissolving of Ag ions and decrease its cytotoxicity.

The morphology of the RD cells cultured on Mg-Zn-Ag metallic glasses for 1 and 2 days is shown in Fig. 15. Compared with the control group, the RD cells cultured on #3-$Mg_{73}Zn_{23}Ag_4$, #4-$Mg_{70}Zn_{26}Ag_4$ and #5-$Mg_{67}Zn_{29}Ag_4$ samples exhibit markedly inhibitory effect after 1 day culturing. When the culturing time extends to 2 days, the RD cells of the control group proliferate obviously, compared with those cultured for 1 day. The RD cells on samples #3-Mg73Zn23Ag4 and #4-Mg70Zn26Ag4 samples exhibit more severe damage features. However, compared with the treated normal MDCK cells, Mg-Zn-Ag metallic glasses exhibit obvious inhibitory effect on RD tumor cells, suggesting its potential application for removal of residual tumor cells.

The analysis on the cyctotoxicity of the Mg-Zn-Ag metallic glasses extracts for RD cells were tested by its 1-fold and 2-fold diluted extracts and their results as shown in Fig. 16. When the culturing time is 2 days, the RD cells in all Mg-Zn-Ag metallic glasses extraction mediums with different dilution ratio exhibit the similar viability. When the culturing time is 4 days, the viability of RD cells in Mg-Zn-Ag metallic glasses extraction mediums with 1:1 dilute ratio decreases greatly. These results indicated that metallic glasses extracts

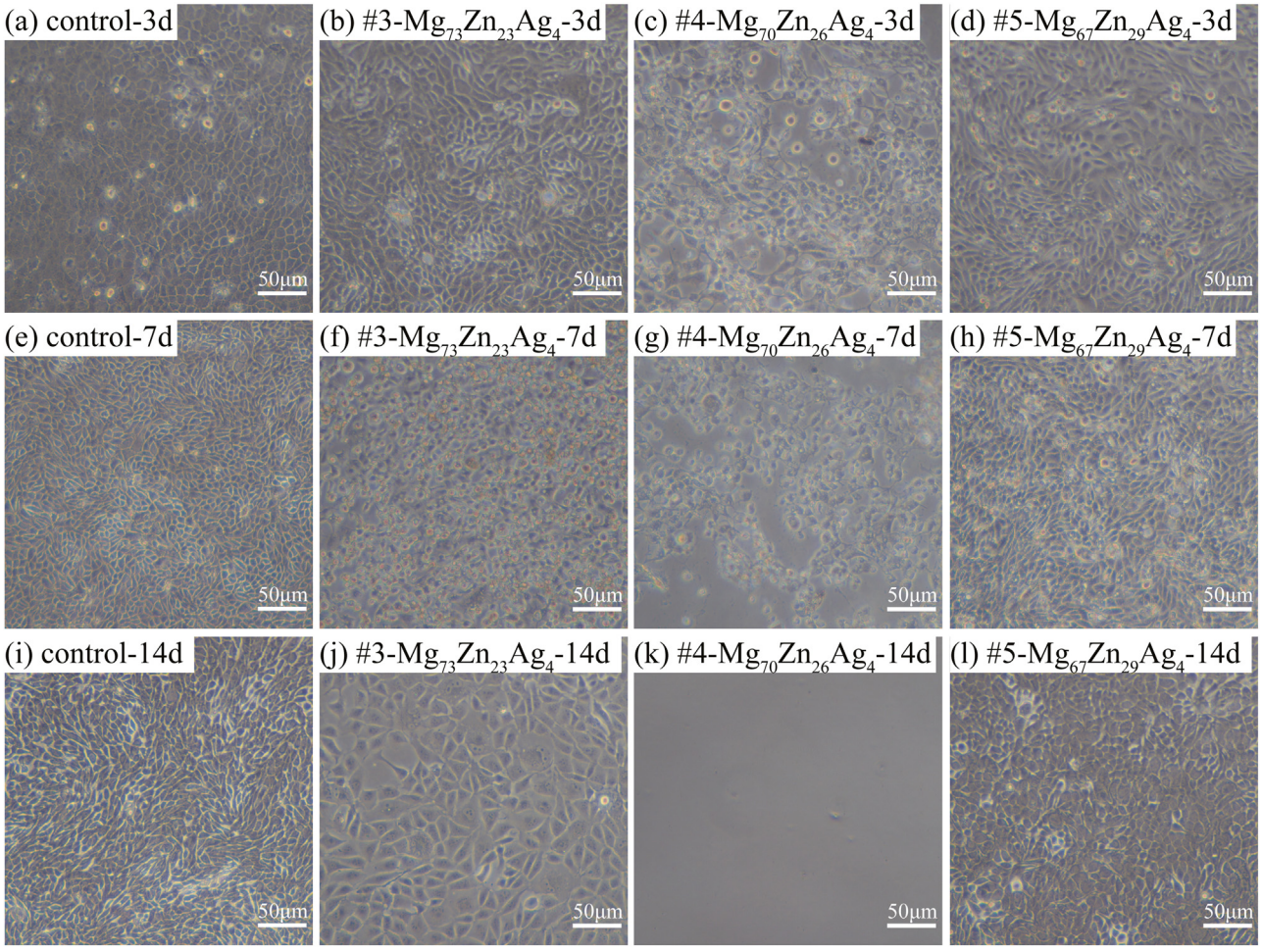

Fig. 13. The morphology of the MDCK cells cultured on Mg-Zn-Ag metallic glasses for 3, 7 and 14 days.

may have obvious inhibitory effect on RD cells proliferation. However, the RD cells in Mg-Zn-Ag metallic glasses extraction mediums with 1:2 dilute ratio exhibit the similar viability, compared with those cultured in extraction mediums with same dilute ratio for 2 days, except the #5-$Mg_{67}Zn_{29}Ag_4$ extraction medium. Such results indicate the ion concentration could affect the tumor cell viability.

The present studied $Mg_{67}Zn_{29}Ag_4$ metallic glass has a relative lower corrosion rate by comparison compared to the previous reported results [44,48-51] (see Fig. 17). The corrosion rate of the $Mg_{67}Zn_{29}Ag_4$ metallic glass is lower than that of the $Mg_{66}Zn_{30}Ca_4$ bulk metallic glass (BMG) and the extruded WE43 alloy. Moreover, it could be found that in the typical biomedical Mg based alloy, the Zn, Al and rare-earth (RE) additions in the Mg alloy could improve the corrosion resistance, while the Ca addition increases the corrosion rate. Such a phenomenon should be attributed to the strengthening effect of alloying elements on the grain boundary. Generally, to obtain the ideal Mg alloy with balanced mechanical properties, the processing technique with grain refinement effect is always the optimum choice. The previous researches [52,53] have demonstrated that the grain size could exert significant influence on the corrosion behavior. With the decrease of grain size, the increased low angel grain boundary would improve the stress corrosion resistance and benefit the service life of the implant [54]. Moreover, the segregated alloying elements of along with grain boundary could help to restrict the corrosion of grain boundary and improve the homogeneous degradation of Mg alloy [55].

For the present fabricated Mg-Zn-Ag metallic glasses, its well homogeneously distributed elements eliminate the pit corrosion. The amorphous crystal structure reduces the corrosion preference of grain boundary, which ensures the uniform degradation. Moreover, the appropriate addition Zn and Ag increase the integral electrode potential of the Mg-Zn-Ag metallic glasses, which enhance the corrosion resistance [3]. Furthermore, the complementary formation of $Zn(OH)_2$ in the corrosion product layer would repair the micro-void and keep its continuous and uniform cover state, which could handicap the subsequent corrosion and ion release. The Zn also prefers to segregate along the crack region of corrosion product layer demonstrate its secondary repairing effect. Therefore, the ions of Zn and Ag are almost no detected in the immersion solution, because they may lie in the corrosion product layer. Such features not only improve the corrosion resistance but also optimize the biocompatibility and antibacterial function

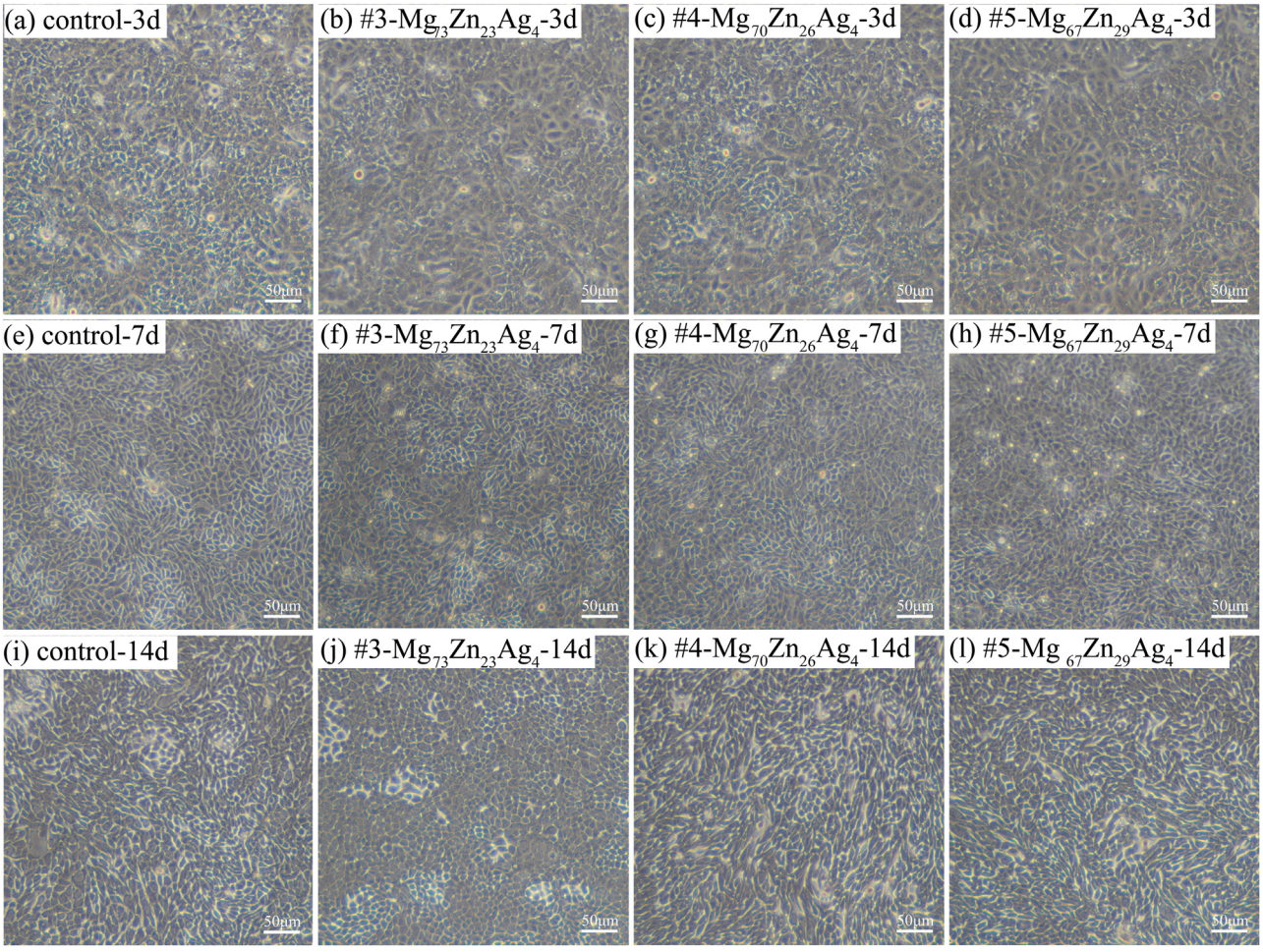

Fig. 14. The morphology of MDCK cells cultured in Mg-Zn-Ag metallic glasses extraction medium for 3, 7 and 14 days.

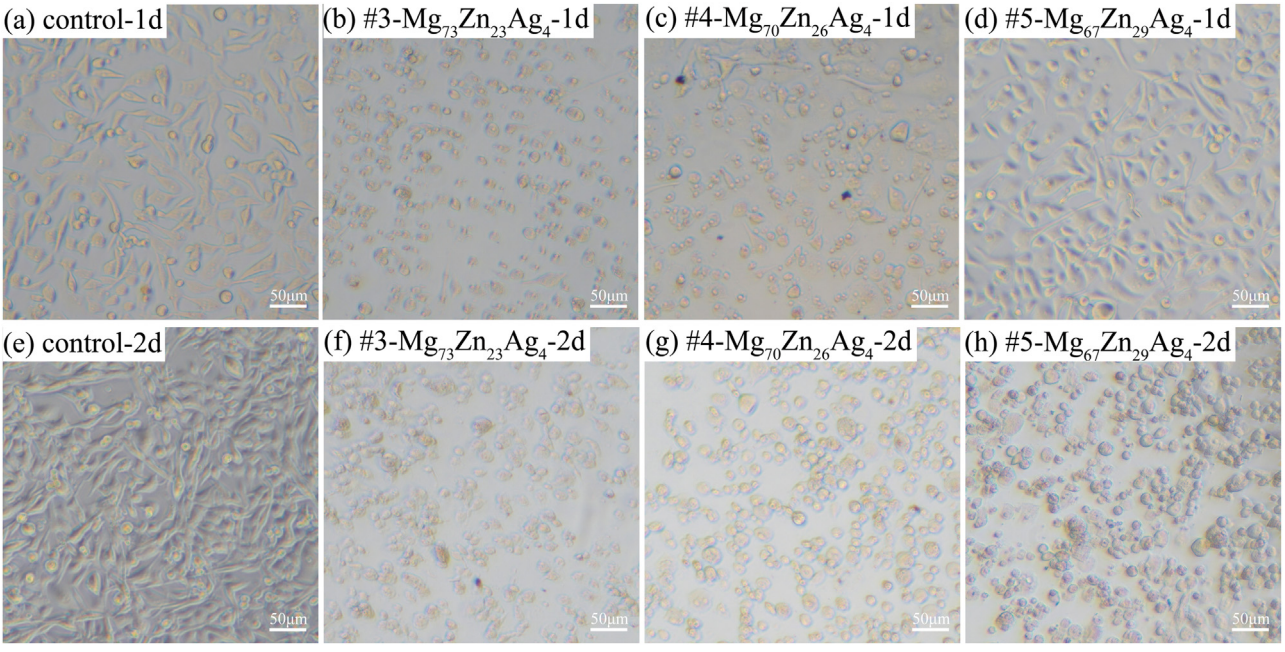

Fig. 15. The comparison of corrosion behavior among Mg67Zn29Ag4 metallic glasses as well as the as reported typical biomedical Mg alloys.

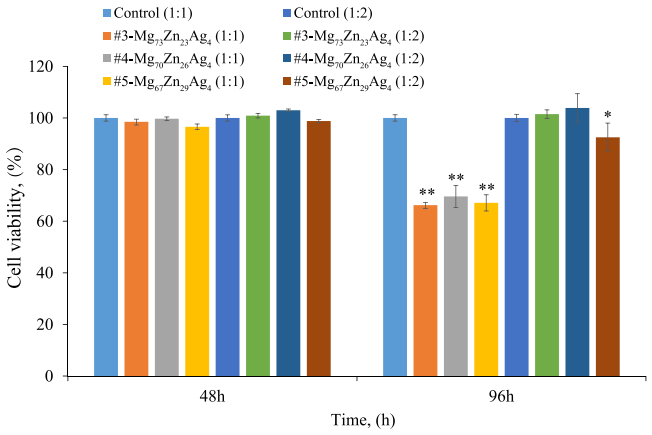

Fig. 16. The RD cells activity cultured in the Mg-Zn-Ag metallic glasses extraction medium using 1-fold and 2-fold diluted extracts (mean ± SD, $^{*}P<0.05$, $^{**}P<0.01$).

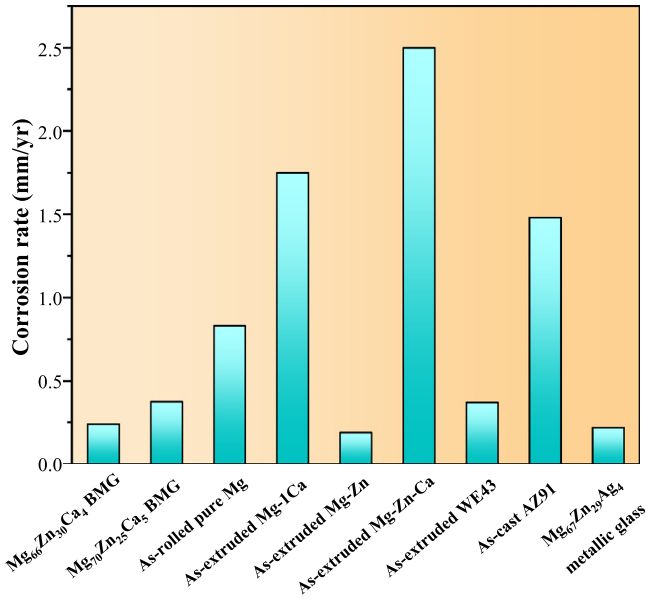

Fig. 17. The comparison of corrosion behavior among Mg67Zn29Ag4 metallic glasses as well as the as reported typical biomedical Mg alloys.

of the Mg-Zn-Ag metallic glasses. The appropriate existence of Ag could significantly reduce the inflammation resulted by the bacterial infection at the initial implanting stage [56,57]. Additionally, the low corrosion rate of Mg-Zn-Ag metallic glasses and enfolded feature of Ag ensure the low releasing rate of Ag ion, which would exert little influence on the biocompatibility of implants fabricated by the Mg-Zn-Ag metallic glasses. Most of all, the Mg and Zn have been proved to be helpful the osteogenesis and angiogenesis [58]. Especially for the bone tissue repair filler, the low corrosion rate and well functionalized Mg-Zn-Ag metallic glasses would be more suitable as the main constituents.

4. Conclusion

In the present research, the systematic investigations have performed on glass forming ability, corrosion behavior and cytocompatibility of the Mg-Zn-Ag metallic glasses to reveal their biomedical application possibility. The following conclusions can be drawn:

(1) The maximum Ep obtained from sample #5-$Mg_{67}Zn_{29}Ag_4$ indicates the best thermal stability of metallic glasses compared to other samples. The maximum T_{rg} was found to be 0.525 at a composition close to $Mg_{67}Zn_{29}Ag_4$, resulting in the best glass-forming ability
(2) The corrosion rate of Mg-Zn-Ag metallic glasses after immersion in SBF solution decreases with the increase of Zn content. The degradation rate of Mg-Zn-Ag metallic glasses meets the clinical application requirement. In addition, the pH and Mg ion concentration decrease with the increase of Zn content.
(3) The MDCK cells cultured in sample #5-$Mg_{67}Zn_{29}Ag_4$ exhibited better cell viability. In addition, the Mg-Zn-Ag metallic glasses exhibit obvious inhibitory effect on RD tumor cells. The well decreased corrosion rate of the Mg-Zn-Ag metallic glasses cooperated with its osteogenesis and tumor inhibition function could benefit its biomedical application as bone tissue repairing filling constituent.

Declaration of Competing Interest

The authors declare that they have no known competing financial interests or personal relationships that could have appeared to influence the work reported in this paper.

Acknowledgements

The authors are grateful to the National Key Research and Development Program of China (2018YFC1106702), Guangdong Basic and Applied Basic Research Foundation (2020A1515011301, 2019A1515110067 and 2020A1515110055), Shenzhen Basic Research Project (JCYJ20210324120001003, JCYJ20200109144608205 and JCYJ20200109144604020) and IER Foundation (HT-JD-CXY-201902 and HT-JD-CXY-201907) for financial support.

Supplementary materials

Supplementary material associated with this article can be found, in the online version, at doi:10.1016/j.jma.2022.09.025.

References

[1] Y. Chen, Z. Xu, C. Smith, J. Sankar, Acta Biomater 10 (11) (2014) 4561–4573.
[2] G.R. Argade, S.K. Panigrahi, R.S. Mishra, Corros Sci 58 (2012) 145–151.
[3] Y. Liu, Y. Zheng, X.H. Chen, J.A. Yang, H. Pan, D. Chen, L. Wang, J. Zhang, D. Zhu, S. Wu, K.W.K. Yeung, R.C. Zeng, Y. Han, S. Guan, Adv Funct Mater 29 (18) (2019).

[4] J. Hofstetter, E. Martinelli, S. Pogatscher, P. Schmutz, E. Povoden-Karadeniz, A.M. Weinberg, P.J. Uggowitzer, J.F. Loffler, Acta Biomater 23 (2015) 347–353.
[5] X. Zhang, J. Dai, Q. Dong, Z. Ba, Y. Wu, J Biomed Mater Res B Appl Biomater 108 (3) (2020) 698–708.
[6] J. Kubasek, D. Vojtech, J Mater Sci Mater Med 24 (7) (2013) 1615–1626.
[7] H.R. Bakhsheshi-Rad, E. Hamzah, A. Fereidouni-Lotfabadi, M. Daroonparvar, M.A.M. Yajid, M. Mezbahul-Islam, M. Kasiri-Asgarani, M. Medraj, Mater Corros 65 (12) (2014) 1178–1187.
[8] J. Du, A. Zhang, Z. Guo, M. Yang, M. Li, S. Xiong, Intermetallics 95 (2018) 119–129.
[9] Z. Zhang, Q. Zhang, L. Jin, Y. Zhang, T. Cai, L. Zhao, J. Wang, Z. Jin, L. Sheng, J Alloys Compd 818 (2020).
[10] J. Wang, Z. Zhang, S. Li, L. Meng, Z. Cao, W.-f. Rao, Calphad 75 (2021).
[11] J. Wang, D. Han, Z. Zhang, I.-.H. Jung, W.-f. Rao, J Chem Thermodyn 163 (2021).
[12] J. Wang, Y.-.N. Zhang, P. Hudon, P. Chartrand, I.-.H. Jung, M. Medraj, J Mater Sci 50 (23) (2015) 7636–7646.
[13] J. Wang, L. Meng, Z. Zhang, B. Sa, X. Fu, L. Sheng, D. Xu, Y. Zheng, J Magnesium Alloys (2021).
[14] J. Wang, Y.N. Zhang, P. Hudon, I.H. Jung, P. Chartrand, M. Medraj, Mater Des (2015).
[15] P. Yin, L. Liu, N. Li, C. Ouyang, T. Lei, J Mater Sci-Mater Med 24 (6) (2013) 1365–1373.
[16] K. Hondo, J. Kaneko, M. Sugamata, M. Kubota, Mater Sci Forum 419-422 (2003) 733–738.
[17] J. Wang, Z. Zhang, Y. Zhang, L. Jin, L. Sheng, J Magnesium Alloys (2021).
[18] Y. Nie, J. Dai, X. Li, X. Zhang, J Magnesium Alloys 9 (4) (2021) 1123–1146.
[19] M. Deng, L. Wang, D. Hoche, S.V. Lamaka, C. Wang, D. Snihirova, Y. Jin, Y. Zhang, M.L. Zheludkevich, Mater Horiz 8 (2) (2021) 589–596.
[20] Y. Zhang, J. Xu, Y.C. Ruan, M.K. Yu, M. O'Laughlin, H. Wise, D. Chen, L. Tian, D. Shi, J. Wang, S. Chen, J.Q. Feng, D.H. Chow, X. Xie, L. Zheng, L. Huang, S. Huang, K. Leung, N. Lu, L. Zhao, H. Li, D. Zhao, X. Guo, K. Chan, F. Witte, H.C. Chan, Y. Zheng, L. Qin, Nat Med 22 (10) (2016) 1160–1169.
[21] W.H. Wang, C. Dong, C.H. Shek, Mater Sci Eng: R: Rep 44 (2–3) (2004) 45–89.
[22] A. Gebert, U. Wolff, A. John, J. Eckert, L. Schultz, Mater Sci Eng A 299 (2001) 125–135.
[23] H.Q. Tang, H.J. Feng, J.H. Zheng, J. Zhao, Surf Coat Technol 201 (9–11) (2007) 5633–5636.
[24] J. Wang, Z. Zhang, I.-.H. Jung, W.-.F. Rao, Intermetallics 136 (2021).
[25] K. Hashimoto, H. Habazaki, E. Akiyama, H. Yoshioka, J.H. Kim, P.Y. Park, Sci Rep Res Inst, Tohoku Univ. Ser. A, Phys, Chem Meta 42 (1996) 99–105.
[26] G. Ben-Hamu, D. Eliezer, A. Kaya, Y.G. Na, K.S. Shin, Mater Sci Eng: A 435-436 (2006) 579–587.
[27] L.-q. Wang, G.-w. Qin, S.-n. Sun, Y.-p. Ren, S. Li, Trans Nonferrous Metals Soc China 27 (12) (2017) 2607–2612.
[28] C. Xiao, X.Y. Shi, W.T. Yu, X.W. Wei, L.L. Cheng, X. Qiu, B.R. Li, C. Fan, J.L. Li, X.Z. Zhang, W. Zhao, Mater Sci Eng C Mater Biol Appl 119 (2021) 111435.
[29] M. Watroba, W. Bednarczyk, J. Kawalko, P. Bala, Bioact Mater 6 (10) (2021) 3424–3436.
[30] B. Du, Z. Hu, J. Wang, L. Sheng, H. Zhao, Y. Zheng, T. Xi, Bioact Mater 5 (2) (2020) 219–227.
[31] B.J. Wang, D.K. Xu, X. Cai, Y.X. Qiao, L.Y. Sheng, J Magnesium Alloys 9 (2) (2021) 560–568.
[32] J. Wang, Z. Zhang, I.-.H. Jung, L. Sheng, Calphad 72 (2021).
[33] C. Wang, Y. Shuai, Y. Yang, D. Zeng, X. Liang, S. Peng, C. Shuai, J Alloys Compd 897 (2022).
[34] J. Wang, Z. Zhang, Y.-.N. Zhang, D. Han, L. Jin, L. Sheng, P. Chartrand, M. Medraj, Mater Lett 256 (2019).
[35] A. Calka, M. Madhava, D.E. Polk, B.C. Giessen, Scripta Metallurgica 11 (1) (1977) 65–70.
[36] Takeshi Matsuda, U. Mizutani, Solid State Commun 44 (2) (1982) 145–149.
[37] H.E. Kissinger, Anal Chem 29 (1957) 1702–1706.
[38] Y.N. Zhang, G.J. Rocher, B. Briccoli, D. Kevorkov, X.B. Liu, Z. Altounian, M. Medraj, J Alloys Compd 552 (2013) 88–97.
[39] A. Hirata, P. Guan, T. Fujita, Y. Hirotsu, A. Inoue, A.R. Yavari, T. Sakurai, M. Chen, Nat Mater 10 (1) (2011) 28–33.
[40] M. Erinc, W.H. Sillekens, R. Mannens, R.J. Werkhoven, Magnesium Technology editors, 2009, pp. 209–214. San Francisco.
[41] M. Cihova, E. Martinelli, P. Schmutz, A. Myrissa, R. Schaublin, A.M. Weinberg, P.J. Uggowitzer, J.F. Loffler, Acta Biomater 100 (2019) 398–414.
[42] J. Wang, P. Chen, L. Meng, L. Jin, Adv Eng Mater (2022).
[43] M. Bornapour, M. Celikin, M. Pekguleryuz, Mater Sci Eng C Mater Biol Appl 46 (2015) 16–24.
[44] X. Gu, Y. Zheng, S. Zhong, T. Xi, J. Wang, W. Wang, Biomaterials 31 (6) (2010) 1093–1103.
[45] P. Monika, V. Adam, Microchem J 134 (2017) 197–201.
[46] A. Oyane, H.-.M. Kim, T. Furuya, T. Kokubo, i. Miyazak, T. Nakamura, J Biomed Mater Res Part A 65A (2) (2002) 188–195.
[47] G. Calabrese, S. Petralia, D. Franco, G. Nocito, C. Fabbi, L. Forte, S. Guglielmino, S. Squarzoni, F. Traina, S. Conoci, Mater Sci Eng C Mater Biol Appl 118 (2021) 111394.
[48] Z. Li, X. Gu, S. Lou, Y. Zheng, Biomaterials 29 (10) (2008) 1329–1344.
[49] S. Zhang, X. Zhang, C. Zhao, J. Li, Y. Song, C. Xie, H. Tao, Y. Zhang, Y. He, Y. Jiang, Y. Bian, Acta Biomater 6 (2) (2010) 626–640.
[50] H.X. Wang, S.K. Guan, X. Wang, C.X. Ren, L.G. Wang, Acta Biomater 6 (5) (2010) 1743–1748.
[51] F. Witte, N. Hort, C. Vogt, S. Cohen, K.U. Kainer, R. Willumeit, F. Feyerabend, Curr Opin Solid State Mater Sci 12 (5–6) (2008) 63–72.
[52] B.N. Du, Z.Y. Hu, L.Y. Sheng, D.K. Xu, Y.X. Qiao, B.J. Wang, J. Wang, Y.F. Zheng, T.F. Xi, J Mater Sci Technol 60 (2021) 44–55.
[53] A. Atrens, Z. Shi, S.U. Mehreen, S. Johnston, G.-.L. Song, X. Chen, F. Pan, J Magnesium Alloys 8 (4) (2020) 989–998.
[54] W. Xu, Y.C. Xin, B. Zhang, X.Y. Li, Acta Mater 225 (2022).
[55] W. Wang, H. Wu, R. Zan, Y. Sun, C. Blawert, S. Zhang, J. Ni, M.L. Zheludkevich, X. Zhang, Acta Biomater 107 (2020) 349–361.
[56] D. Tie, F. Feyerabend, W.D. Muller, R. Schade, K. Liefeith, K.U. Kainer, R. Willumeit, Eur Cell Mater 25 (2013) 284–298 discussion 298.
[57] G. Jin, H. Qin, H. Cao, S. Qian, Y. Zhao, X. Peng, X. Zhang, X. Liu, P.K. Chu, Biomaterials 35 (27) (2014) 7699–7713.
[58] J. Wang, J. Xu, X. Wang, L. Sheng, L. Zheng, B. Song, G. Wu, R. Zhang, H. Yao, N. Zheng, M.T. Yun Ong, P.S. Yung, L. Qin, Biomaterials 268 (2021) 120576.